Available online at www.sciencedirect.com

SCIENCE DIRECT®

International Journal of Heat and Fluid Flow 27 (2006) 351–370

International Journal of HEAT AND FLUID FLOW

www.elsevier.com/locate/ijhff

Detached eddy simulation of flow and heat transfer in fully developed rotating internal cooling channel with normal ribs

Aroon K. Viswanathan, Danesh K. Tafti *

Mechanical Engineering Department, Virginia Polytechnic Institute and State University, 114-I Randolph Hall, Mail Code 0238, Blacksburg, VA 24061, USA

Received 13 May 2005; received in revised form 28 October 2005; accepted 29 December 2005

Abstract

Numerical predictions of a hydrodynamic and thermally developed turbulent flow are presented for a rotating duct with square ribs aligned normal to the main flow direction. Three rotation numbers $Ro = 0.18$, 0.35 and 0.67 are investigated. The rib height to channel hydraulic diameter (e/D_h) is 0.1, the rib pitch to rib height (P/e) is 10 and the calculations have been carried out for a bulk Reynolds number of 20,000. The capability of the detached eddy simulation (DES) in predicting the turbulent flow field and the heat transfer under the effects of rotation has been evaluated against unsteady Reynolds-averaged Navier Stokes (URANS), large-eddy simulations (LES), and experimental data. It is shown that DES by capturing a large portion of the turbulent energy in the resolved scales is much more capable than URANS in transcending the underlying shortcomings of the RANS model. DES shows much better fidelity in calculating critical components of the turbulent flow field and heat transfer than URANS.

Keywords: Detached eddy simulations (DES); Ribbed ducts; Turbine blade internal cooling; Coriolis forces; Turbulence

---

1. Introduction

The flow behind a rib (turbulator) though geometrically simple, has some complex features: separation of the boundary layer, a curved shear layer, primary and secondary recirculation, reattachment of the boundary layer, recovery, etc. These complex features of the flow pose a big challenge in the numerical prediction of the flow behind the rib. Studies on backward facing step (Driver and Seegmiller, 1985; Amano and Goel, 1995) show that the turbulent viscosity and the turbulent shear stress are usually over-predicted by the two equation models in such cases. This results in the rapid spreading of the shear layer due to which the reattachment is predicted early. Speziale and Ngo (1988) theoretically proved the ineffectiveness of the linear two equation models. They showed the serious inaccuracies that rise in the case of a backward facing step.

Rotation (or streamline curvature) generates an extra strain rate that tends to significantly affect the stress production. Bradshaw (1969) formulated an analogy between meteorological parameters and the parameters describing rotation about the axis normal to the plane of rotation. Bradshaw defined an effective Richardson number for flows undergoing rotation which is linearly related to the mixing length. Most of the later studies also propose a similar definition. Bradshaw (1988) and Ishigaki (1996) discuss the analogy between the effects induced by curvature and orthogonal rotation in turbulent flows. When the direction of rotation is in tandem with the angular velocity (or in a flow over a concave surface) the flow is unstable while the flow is stable if the directions are opposing (convex surface). Linear eddy viscosity models fail to account for these effects because of the inability to reproduce normal stresses that appear in the production term. So these effects are

---

* Corresponding author. Tel.: +1 540 231 9975; fax: +1 540 231 9100.
E-mail address: dtafti@vt.edu (D.K. Tafti).

0142-727X/$ - see front matter © 2006 Elsevier Inc. All rights reserved.
doi:10.1016/j.ijheatfluidflow.2005.12.003

Nomenclature

Bo	Buoyancy number ($=\Delta\rho/\rho \cdot r/D_h \cdot Ro^2$)
D_h	hydraulic diameter used as characteristic length scale for presenting all results in non-dimensional form
e	rib height
k	thermal conductivity (W/mK)
$\vec{n}$	surface normal vector
P	total pressure or rib pitch
p	fluctuating, modified or homogenized pressure
Pr	Prandtl number ($=\mu C_p/k$)
q''	constant heat flux boundary condition on duct walls and rib
Re	Reynolds number based on bulk velocity ($=\bar{u}_b D_h/\nu$)
Ro	rotation number based on bulk velocity ($=\omega_z D_h/\bar{u}_b$)
f	fanning friction factor
Nu	local Nusselt number ($Nu = 1/(\theta_s - \theta_{ref})$)
$\langle Nu \rangle$	spatially averaged Nusselt number ($\langle Nu \rangle = (\int\int_A 1/(\theta_s - \theta_{ref})\,dA)/(\int\int_A dA)$)
TKE	turbulent kinetic energy
t_{LES}	fraction of time when the region is evaluated in SGS mode
$\vec{u}$	Cartesian velocity vector
u_b	mean bulk velocity used as characteristic velocity for presenting all results in non-dimensional form

X, Y, Z, x, y, z	physical coordinates
β	non-dimensional mean pressure gradient
β^*	modeling constant in the SST equation
Δ	grid length scale ((+) wall normal direction, ($\|\|$) wall parallel direction)
δ	Kronecker delta
ε_{ijk}	permutation tensor
γ	mean temperature gradient
κ	non-dimensional frequency
θ_s	non-dimensional surface temperature
θ_{ref}	non-dimensional reference temperature ($\theta_{ref} = (\int\int_{A_x} \|u\theta\| \cdot dA_x)/(\int\int_{A_x} \|u\| \cdot dA_x)$)
ω	specific dissipation rate of TKE
ω_z	angular velocity of rotation (rad/s) about z-axis
$\vec{\xi}$	computational coordinates

Subscripts

b	bulk
o	smooth duct
s	surface
t	turbulent parameters
τ	parameters based on friction velocity

modeled by ad hoc corrections using a rotation Richardson number.

Wilcox and Chambers (1977) proposed a modified version of the k–ε equation, where they modeled the Coriolis term in the k-equation as a function of the rotation of the system. The model was applied for rotating channel flow and cases with streamline curvature. The predictions were within 10% of the measured results. Launder et al. (1977) applied the effects of curvature by making one of the coefficients in the transport equation for ε a function of the rotational Richardson number ($C_c = C_2(1 - 0.2Ri_t)$). The model was applied to a variety of boundary layer flows developing over spinning and curved surfaces. The agreement was only satisfactory but better than that under conditions when rotational effects were not modeled.

Howard et al. (1980) used Wilcox's model (1977) and Launder's model (1977) to compute the flow in high and low aspect ratio ducts. For the high aspect ratio duct case the simulation was carried out for rotation numbers ranging from $Ro = 0$–0.42. Launder's model was observed to get unstable for high rotation numbers. All the comparisons moderately agreed with the experimental results but were not accurate. For the low aspect ratio case it was observed that the predicted velocity profiles did not agree quantitatively with the experiments although the shape of the profile was correctly predicted. Rodi and Scheuerer (1983) used extensions of k–ε models – an Algebraic Stress Model and two modified versions of ε equation proposed by Launder et al. (1977) and Hanjalic and Launder (1980), to predict flows in a curved boundary layer, a curved mixing layer and a curved wall jet. It was observed that with curvature corrections the flow in the separated region was accurately captured. However the flow predictions in the recovery region were incorrectly predicted by all the models.

Chima (1996) proposed a modified two equation k–ω turbulence model by writing the production terms in both the k and the ω equations in terms of vorticity. The model was applied to transonic flows over a flat plate, over a compressor and over a turbine vane. The results compared well with the experiments but were not substantially better than the computations using Baldwin–Lomax model for the cases considered.

Hellsten (1998) suggested improvements in the k–ω SST model (Menter, 1992, 1993) to make it rotationally invariant, by modifying the coefficient of the production term in the k-equation. The production term was divided by a factor ($=1 + C_{rc}Ri$) to incorporate the effects of rotation. The model was tested for a spanwise rotating channel. It was observed that for high rotation numbers ($Ro = 0.21$, 0.42), the maximum velocity point is predicted too near the suction side wall. Schweighofer and Hellsten (1999) used the model to study the flow around a HSVA-1 tanker. However the effect of the rotation–curvature correction was small since the radius of curvature of the hull was quite large compared to the boundary layer thickness. Also the correction seemed to have a minor impact on the results in many of the other cases (personal communication).

2. Numerical modeling of flow in rotating internal cooling ducts

A numerical study of fully developed flow in a rotating rectangular duct was performed by Iacovides and Launder (1991). Ducts with a square cross-section and with an aspect ratio of 2:1 were studied. The Reynolds number varied from 33,500 to 97,000 and the rotation number ranged from 0.005 to 0.2. The standard high Reynolds number k–ε model was used for the bulk of the flow. Near the wall, a low Reynolds number one-equation model was used. The calculations correctly predicted the secondary flow caused by Coriolis forces. However, there was only a qualitative match between the computed and experimental heat transfer results.

Bo et al. (1995) studied developing flow in an orthogonally rotating square duct. The rotation numbers were 0.12 and 0.24. Three turbulence models were used in the analysis: a k–ε eddy viscosity model (EVM) with a low Reynolds number one-equation EVM near the wall, a low Reynolds number algebraic stress model (ASM), and a low Reynolds number k–ε EVM. Results from the low-*Re* k–ε EVM for both constant and variable density were very unrealistic and were not pursued any further. The k–ε/one-equation EVM generally performed well for low rotation, but results deviated substantially from experimental results on both leading and trailing sides for the high rotation number case. These discrepancies occurred whether buoyancy was considered or not. The low-*Re* ASM performed the best of all, matching the data reasonably well when buoyancy effects were considered. However, results deviated significantly from experimental data for x/D_h greater than 5 in almost every calculation.

Prakash and Zerkle (1995) used the standard k–ε model to simulate outward flow and heat transfer in a smooth square duct with radial rotation. Coriolis and buoyancy forces were included only in the mean equations. The Reynolds number was kept at 25,000 and the rotation numbers were 0.24 and 0.48. Simulations were done for buoyancy numbers of 0.01 and 0.13. The low buoyancy number simulations did not match trends from experimental data. However, results from the high buoyancy number simulations were in qualitative agreement with experimental data. The authors attributed the quantitative disagreement to the need for including rotation and buoyancy effects in the k–ε model.

Rigby (1998) used Chima's k–ω model to predict the flow in a rotating internal cooling passage with a 180° turn and ribbed walls. Reynolds numbers in the range 5200–7900 were tested for two rotation cases ($Ro = 0$ and 0.24). The predictions for the rotation cases were not accurate. The mass transfer was over predicted in the first leg and was under-predicted in the second leg.

Stephens et al. (1996) used Menter's SST model to compute flow and heat transfer in a rotating U-shaped square duct with smooth walls. No special terms were included for Coriolis and buoyancy forces in the turbulence model. The Reynolds numbers used in the flow are 25,000 and 50,000. Stationary and rotating cases ($Ro = 0.24$, 0.48) were considered. The overall heat transfer was predicted reasonably well by the computations. Lin et al. (2001) studied the three dimensional flow and heat transfer in a U-shaped duct under rotating and non-rotating conditions ($Ro = 0$, 0.24) for a Reynolds number of 25,000 and a density ratio ($\Delta\rho/\rho$) of 0.13. Menter's shear stress model was used for closure. The evolution of flow and the effect of Coriolis forces, centrifugal buoyancy, staggered ribs and the 180° bend were studied. However the average heat transfer augmentation showed only moderate agreement with experimental results.

Large eddy simulations (LES) have been used in the past to study the heat transfer in ribbed channels. Murata and Mochizuki (1999, 2000) studied the effect of Coriolis force and the duct cross-section on the heat transfer in smooth and ribbed channels. Watanabe and Takahashi (2002) carried out LES computations and experimental studies on a rectangular channel with transverse ribs which are heated from one side and got good agreement with the experiments. The studies also revealed the unsteady mechanism that enhanced the heat transfer in the ribbed channel. Tafti (2005) used 96^3 and 128^3 grids to predict the heat transfer in a stationary channel with orthogonal ribs with a pitch to rib height ratio (P/e) of 10 and a rib height to hydraulic diameter (e/D_h) of 0.1. The computations also gave a comprehensive knowledge of the major flow structures in the flow field and compared very well with experiments.

Abdel-Wahab and Tafti (2004a,b) validated the LES Dynamic Smagorinsky model for a ribbed duct with Coriolis and buoyancy forces. Ribs with a $P/e = 10$ and $e/D_h = 0.1$ were studied and some of the hydrodynamic and turbulent characteristics of the flow, which are difficult to obtain through experiments were highlighted. The heat transfer at the leading wall was observed to decrease as the rotational speed increases but increased along the trailing wall of the rotating duct. The computed data compared well with experimental results. LES computations for developing flow and heat transfer in rotating ducts have also been carried out by Sewall and Tafti (2004b, 2006, accepted for publication), with and without the inclusion of centrifugal buoyancy forces.

While accurate results have been obtained with LES computations, the grid requirements are very demanding. The resolution in the boundary layer is fine and the resolution increases with the increase in the Reynolds number. This calls for a special treatment of the boundary layer to limit the number of grid points. One of the several techniques available for wall modeling is detached eddy simulation (DES), which was proposed by Spalart et al. (1997).

DES is a modification of a RANS model in which the model switches to a subgrid scale formulation in regions fine enough for LES calculations. The transition is seamless as a single equation is used to define the LES and the RANS regions of the flow without any explicit declaration of the zones. Thus DES tries to capitalize on the advantages on the RANS model near the boundary and regions of low turbulence where the turbulent length scale is less than the maximum grid dimension. As the turbulent length scale exceeds the grid dimension, the regions are solved using the LES mode. The grid resolution is not as demanding as pure LES, thereby considerably cutting down the cost of the computation. Though DES was initially formulated for the Spalart–Allmaras model, it can be implemented with other RANS models (Strelets, 2001), by appropriately modifying the length scale which is explicitly or implicitly involved in the RANS model. By appropriately designing the grid, the regions of massive separation are computed using LES which ensures that the normal stresses, which are quite significant in this region, are not neglected. So by just switching the mode of computation from URANS to LES in regions of massive separation the performance of the URANS model is enhanced.

In the recent past many calculations applied to external aerodynamic flows have been reported. These computations have accurately captured the flow physics over various complex geometries (Squires et al., 2002; Forsythe et al., 2002; Kapadia et al., 2003). Viswanathan and Tafti (2004, 2005a,c, 2006) used DES to compute flow in an internal cooling duct with normal and skewed ribs. These computations showed that DES while being as accurate as LES was less expensive than LES. The heat transfer and flow characteristics predicted were in good agreement with the experiments and LES computations reported earlier.

3. Objective of the study

The objective of the current study is to assess the capability of DES in capturing the effects of rotation on the flow and heat transfer in a fully developed ribbed channel. To the best of our knowledge this is the first application of DES to an internal non-canonical flow with heat transfer and follows an earlier study in stationary ribbed ducts (Viswanathan and Tafti, 2004, 2005c). Unlike the study by Nikitin et al. (2000) in turbulent channel flows in which the Spalart–Allmaras model was used as a wall model, in the current study the two-equation model behaves as a hybrid RANS-LES model throughout the calculation domain. This paper aims to test the hypothesis as to whether DES can overcome known shortcomings of the underlying RANS model to increase the accuracy of the computation. In this case, it is the inability of eddy-viscosity RANS models to accurately predict the effects of rotation and Coriolis forces on flow structure and heat transfer.

A fully developed flow in a duct with normal ribs of rib pitch-to-height ratio $P/e = 10$ and a rib height to hydraulic diameter ratio $e/D_\mathrm{h} = 0.1$, has been considered. The Reynolds number based on bulk velocity is 20,000. Three rotation numbers $Ro = 0.18$, 0.35 and 0.67 are considered. Since detailed experimental measurements are not available in the literature for rotating ducts, the DES and URANS results are compared with the LES results of Abdel-Wahab and Tafti (2004a,b). However the overall surface averaged heat transfer data is available from the experiments of Wagner et al. (1992), Parsons et al. (1994) and Liou et al. (2001), and hence these are used for comparing the average heat transfer on the ribbed and the side walls.

4. Computational model and governing equations

The computational model which assumes a fully developed flow and heat transfer simulates a periodically repeating spatial unit consisting of two ribs (one on either side of the duct) as shown in Fig. 1(a). Earlier studies (Sewall and Tafti, 2004b, accepted for publication) in a single pass of a rotating internal cooling duct with nine ribs show that the flow and heat transfer in the fully developed region matches well with the fully developed calculation over a single rib pitch (Abdel-Wahab and Tafti, 2004a,b). Hence a single rib pitch is considered to be sufficient for these computations.

The duct walls as well as all six faces of the two ribs exposed to the main flow are heated by imposing a constant heat flux (q'') boundary condition. The duct is subjected to orthogonal rotation with axis along the positive z-direction at an angular velocity ω_z. The governing flow and energy equations are non-dimensionalized by a characteristic length scale which is chosen to be the hydraulic diameter of the channel (D_h), a characteristic velocity scale given by the friction velocity $u_\tau = \sqrt{\Delta \overline{P}_x/\rho}$, and a characteristic temperature scale given by $q''D_\mathrm{h}/k$. The assumed periodicity of the domain in the streamwise or x-direction requires that the mean gradients of pressure and temperature be isolated from the fluctuating periodic component as follows:

$$\begin{aligned} P(\vec{x},t) &= P_\mathrm{in} - \beta x + p(\vec{x},t) \\ T(\vec{x},t) &= T_\mathrm{in} + \gamma x + \theta(\vec{x},t) \end{aligned} \tag{1}$$

where β and γ are mean streamwise pressure and temperature gradients, respectively.

On substitution into the Navier–Stokes and energy equations, the non-dimensional time-dependent equations in transformed coordinates $\vec{\xi} = \vec{\xi}(\vec{x})$ take the following conservative form:[1]

Continuity:

$$\frac{\partial}{\partial \xi_j}\left(\sqrt{g}\overline{U}^j\right) = 0 \tag{2}$$

---

[1] Henceforth, all usage is in terms of non-dimensionalized values.

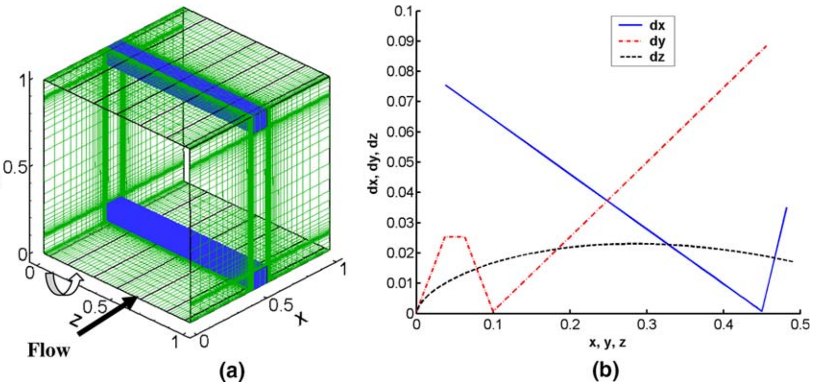

Fig. 1. (a) Schematic diagram representing the grid in the periodic ribbed duct. The system is rotated about the z-axis. (b) Grid distribution in the three directions.

Momentum:

$$\frac{\partial}{\partial t}(\sqrt{g}\bar{u}_i)+\frac{\partial}{\partial \xi_j}(\sqrt{g}\overline{U}^j\bar{u}_i) = -\frac{\partial}{\partial\xi_j}(\sqrt{g}(\vec{a}^j)_i\bar{p}) + \frac{\partial}{\partial\xi_j}\left(\left(\frac{1}{Re_\tau}+\frac{1}{Re_{t_\tau}}\right)\sqrt{g}g^{jk}\frac{\partial\bar{u}_i}{\partial\xi_k}\right) + \sqrt{g}\beta\delta_{i1} - 2(Ro_\tau)\bar{u}_m\epsilon_{i3m} \tag{3}$$

Energy:

$$\frac{\partial}{\partial t}(\sqrt{g}\bar{\theta})+\frac{\partial}{\partial \xi_j}(\sqrt{g}\overline{U}^j\bar{\theta}) = \frac{\partial}{\partial\xi_j}\left(\left(\frac{1}{Pr\,Re_\tau}+\frac{1}{Pr_t\,Re_{t_\tau}}\right)\sqrt{g}g^{jk}\frac{\partial\bar{\theta}}{\partial\xi_k}\right) - \sqrt{g}\gamma\bar{u}_1 \tag{4}$$

where $\vec{a}^i$ are the contravariant basis vectors,[2] $\sqrt{g}$ is the Jacobian of the transformation, g^{ij} is the contravariant metric tensor, $\sqrt{g}U^j = \sqrt{g}(\vec{a}^j)_i u_i$ is the contravariant flux vector, u_i is the Cartesian velocity vector, Ro_τ is the rotation number, and θ is the modified temperature. In Eq. (3), only the rotational Coriolis forces are included in the formulation. The centrifugal forces are combined with the pressure gradient term and centrifugal buoyancy effects are neglected. Turbulence is modeled using Menter's SST model (Menter, 1993) in both the DES and URANS formulations.

5. Detached eddy simulations

In the SST model, the RANS length scale, $l_{k\text{–}\omega}$, which is defined as $l_{k\text{–}\omega} = \sqrt{k}/\beta^*\omega$ is replaced by a DES length scale δ, where $\delta = \min(l_{k\text{–}\omega}, C_{\mathrm{DES}}\Delta)$, $\Delta = \max(\Delta_x, \Delta_y, \Delta_z)$ and the resulting sub-grid model reduces into a Smagorinsky-like model (Strelets, 2001). Based on this, the dissipation term in the k-transport equation is reduced to

$$D^k = (\rho k^{3/2})/\delta$$

In the SST model, the blending function F_1 is used to determine the value of the DES constant.

$$C_{\mathrm{DES}} = (1-F_1)C_{\mathrm{DES}}^{k\text{–}\varepsilon} + F_1 C_{\mathrm{DES}}^{k\text{–}\omega}$$

$$C_{\mathrm{DES}}^{k\text{–}\bar{\omega}} = 0.78 \quad C_{\mathrm{DES}}^{k\text{–}\omega} = 0.61$$

However the k–ε value of the C_{DES} value is encountered more often when the RANS-LES switch takes place. In this paper the term 'RANS mode' is used when DES uses the RANS length scale ($l_{k\text{–}\omega}$) and 'LES mode' when the model behaves as a SGS type model.

6. Numerical method

The governing equations for momentum and energy are discretized with a conservative finite-volume formulation using a non-staggered grid topology. The Cartesian velocities, pressure, and temperature are calculated and stored at the cell center, whereas contravariant fluxes are stored and calculated at the cell faces. Time integration of the discretized continuity and momentum equations is performed via semi-implicit projection method. The temporal advancement is performed in two steps, a predictor step, which calculates an intermediate velocity field, and a corrector step, which calculates the updated velocity at the new time step by satisfying discrete continuity. The energy and turbulence equations are advanced in time using an explicit Adams–Bashforth for the convection terms and Crank–Nicolson for the diffusion terms. A second order central difference scheme is used in the momentum and energy equations. The equations for the turbulent kinetic energy and the dissipation rate are solved using a second order central difference scheme with a TVD limiter.

The computer program GenIDLEST (generalized incompressible direct and large-eddy simulations of turbulence) used for these simulations has been applied extensively to study heat transfer and flow characteristics in internal cooling ducts and various other applications (Sewall and Tafti, 2004a,b, accepted for publication, 2006; Sewall et al., 2006; Abdel-Wahab and Tafti, 2004a,b,c; Viswanathan and Tafti, 2004, 2005a,b,c, 2006; Viswanathan et al., 2005). Details

---

[2] The notation $(\vec{a}^j)_i$ is used to denote the ith component of vector $\vec{a}^j \cdot (\vec{a}^j)_i = \partial\xi_j/\partial x_i$.

about the algorithm, functionality, and capabilities can be found in Tafti (2001).

6.1. Computational details

In this paper, calculations for three rotation numbers $Ro = 0.18$, 0.35 and 0.67 at a nominal bulk Reynolds number of 20,000 are presented. For each rotation number, the computational domain consists of a ribbed channel, with two ribs placed at the center of the channel at the top and the bottom.

LES computations (Tafti, 2005) on stationary ducts were carried out using a 96^3 grid and a 128^3 grid. These computations showed that the dynamic Smagaronsky model on both these grids showed excellent agreement with the experimental results predicting overall heat transfer and friction factors within 10% of the experiments (Rau et al., 1988). The localized flow and heat transfer trends observed at the smooth and the ribbed walls matched well with the experiments. Since these grids have been observed to resolve the flow and heat transfer in a stationary duct accurately, the LES predictions on a 128^3 grid, for a rotating duct (Abdel-Wahab and Tafti, 2004a,b) have been considered to be sufficiently accurate to be taken as the reference for the current DES computations.

While in the turbulent channel computations (Nikitin et al., 2000), a wall boundary condition is applied only in the single wall normal direction (periodicity considered in the streamwise and the spanwise directions), in the present computation wall boundary conditions have to be applied in all three directions (at the duct walls and on the ribs). Hence the grid distribution in all the three directions has to satisfy the required wall normal resolution of the base RANS model. The grid and the coordinate system used are shown in Fig. 1(a). The baseline grid formed consists of 65 nodes in the streamwise direction, of which 13 nodes lie directly over the rib, with 53 nodes in the inter-rib space. In the cross-stream direction the grid consists of 65×65 nodes with 13 nodes each in the regions of the rib, covering the rib height of e and 41 nodes in the middle of the channel and 65 nodes distributed using a monotonic spline distribution along the span. The grid distribution is symmetric in the y and the z directions. DES calculations on a stationary internal cooling duct have been validated against the data of Rau et al. (1988) and found to match the heat transfer augmentation and the friction factor within an experimental uncertainty of ±9%.

A posteriori evaluation of the grid distributions were carried out based on the local friction velocities. The streamwise grid distribution gives $\Delta^+ < 1$ near the ribs and $\Delta^+_{\max} \sim 150$ in the inter-rib space. The spanwise distribution yields $\Delta^+ < 1$ near the side walls and $\Delta^+_{\max} \sim 180$ in the center. While the grid distribution in the wall normal direction ($\Delta^+ \sim 1$–1.25) was similar to the values obtained in the LES computation, the streamwise and the spanwise grids for this grid are more relaxed than the LES computation in which $\Delta^{\|} < 30$. The grid spacings in the x, y, and z directions are shown in Fig. 1(b). This distribution allows a major part of the boundary layer to be treated in the RANS mode. In total, the domain was discretized into 262,144 cells. The domain was divided into eight equal blocks ($64 \times 64 \times 8$ cells) in the spanwise direction to facilitate parallel processing.

A non-dimensional time step of 5×10^{-5} was used in all the 64^3 DES and URANS rotating duct computations. Calculations are initiated by assuming an initial bulk velocity and integrating in time until a balance between the internal losses and the specified pressure gradient is obtained. Time evolution of the bulk quantities are monitored and the solution is allowed to reach a statistically steady state and adjust to the new set of conditions for around five non-dimensional time units. The mean characteristics of the flow are calculated by averaging the solution for an additional five time units. Although the whole domain is considered for the calculation, owing to the symmetry along the z-direction, the average solution for half the domain is presented.

To calculate the augmentation ratio, reference values for Nusselt number and friction factor for a smooth duct are obtained from the correlations (Incropera and Dewitt, 2002).

$$Nu_0 = 0.023 \cdot Re_{\mathrm{b}}^{0.8} \cdot Pr^{0.4}$$

$$f_0 = 0.046 \cdot Re_{\mathrm{b}}^{-0.2}$$

The predicted heat transfer results are compared with data of Liou et al. (2001), Wagner et al. (1992) and Parsons et al. (1994).

All results are presented in non-dimensional form using the bulk mean velocity as the characteristic velocity and the hydraulic diameter of the duct as the characteristic length scale.

7. Results

7.1. Grid sensitivity

The grid required for a DES calculation is dependent on the underlying RANS model and the flow physics. While in the Spalart–Allmaras model, the switch from RANS to LES is only dependent on the grid distribution in the near wall region, and which only happens once, in the k–ω based models, RANS and LES regions can be interspersed in the calculation domain depending on the grid and the turbulent characteristics of the flow. The model ceases to act only as a wall model but models turbulence wherever the grid resolution is not enough to resolve the turbulence. Hence in the limit of a coarse grid, the solution procedure will default to URANS and in the fine limit to a LES. Hence the grid should strike a balance between a LES in critical regions and RANS in not so critical regions, with the intent to emulate the accuracy of LES at a lower computational cost. Computations were carried out for a stationary duct for a fully developed case on three grids:

48^3, 64^3 and 96^3. Fig. 2 shows the comparison of the streamwise velocities for a stationary duct at a plane ($Y/e = 0.25$) passing through the rib, as predicted by the different grids used in comparison with the LES results on a 128^3 grid. The coarse grid (48^3) failed to capture the secondary reverse flow behind the rib, owing to the dominance of RANS in the solution. The 64^3 and the 96^3 grids predicted the trends accurately. The 96^3 grid did not show any added value, and so the 64^3 grid was considered to be sufficiently accurate for the rotating cases. Using the same argument, DES computations (Viswanathan and Tafti, 2004, 2005c) were carried out for a stationary fully developed ribbed duct on the 64^3 grid. The results showed good agreement with the LES computations and the experiments. Hence the DES and the URANS calculations for the rotation cases are also carried out on the 64^3 grid.

While the 64^3 grid is observed to be appropriate for DES, the resolution is not sufficient for LES. A comparison of the reattachment lengths downstream of the rib for a stationary duct shows that the LES on a 128^3 grid and DES on the 64^3 grid predict a reattachment length of around 4.1 times the rib height, which is in good agreement with the experimental measurements on 4.1–4.25 by Rau et al. (1988). On the other hand, LES on the 64^3 grid predicts a reattachment length of 3.7. Fig. 3 shows the comparison of the heat transfer augmentation at the ribbed and the side walls of a stationary duct with ribs normal to the flow direction. A comparison of the ribbed wall heat transfer augmentation shows that while the 128^3 LES, 96^3 LES and 64^3 DES predict heat transfer augmentation consistent with the heat transfer measured by Rau et al. (1988), 64^3 LES over-predicts the heat transfer in the separated region. A comparison of the side wall heat transfer also shows that the heat transfer in the vicinity of the rib ($y < 0.1$) is over-predicted by 64^3 LES. The predictions by 64^3 DES and 128^3, 96^3 LES in this region are in good agreement with the values measured by the experiments. The under-prediction of the reattachment length and the

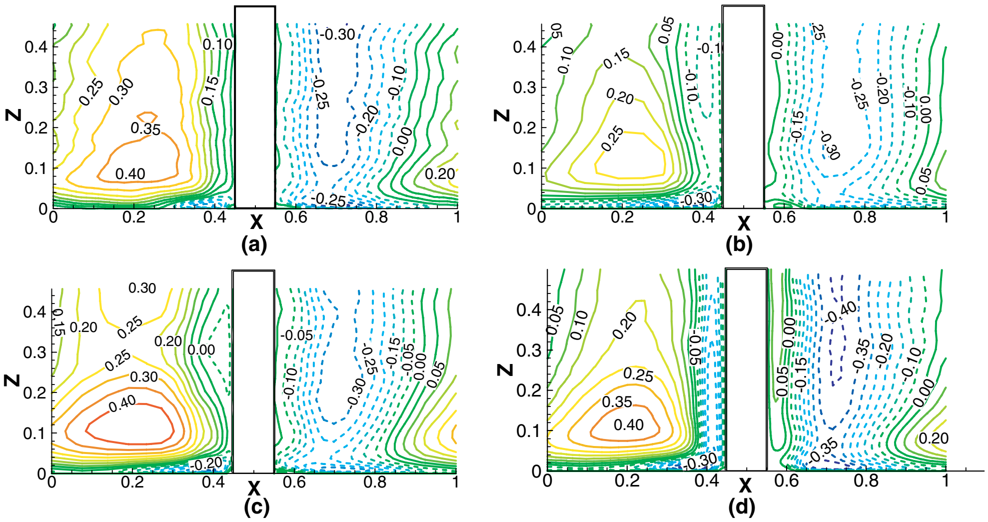

Fig. 2. Comparison of the streamwise velocity contours at $Y/e = 0.25$ plane. (a) LES 128^3; (b) DES 48^3; (c) DES 64^3; (d) DES 96^3. Flow direction is from left to right.

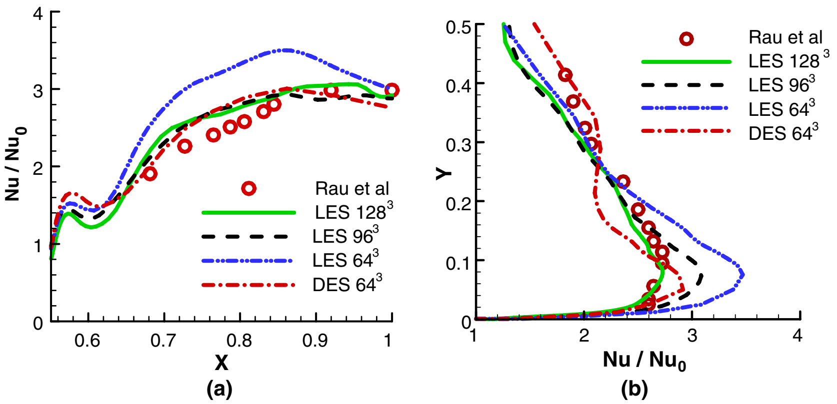

Fig. 3. Comparison of the heat transfer predictions. (a) Ribbed wall heat transfer downstream of the rib ($z = 0.5$). (b) Side wall heat transfer comparison ($x = 0.40$).

over-prediction of the heat transfer in the region is a result of the coarser grid resolution in the 64^3 grid. Similar trends were observed for the rotation cases, where the reattachment lengths at the trailing and the leading sides were under-predicted and the heat transfer augmentations were over-predicted at the ribbed walls. In general the quality of the results is observed to deteriorate with LES as the grid is coarsened to 64^3. Thus it is inferred that the 64^3 grid used is not sufficient for an accurate LES computation, while the grid when used for DES is capable of yielding results comparable in accuracy to the LES computations.

7.2. DES regions

Fig. 4(a) shows the fraction of time (during the whole computation) when the calculation is solved in the LES mode. DES with Menter's SST model uses a turbulent length scale which is computed from the turbulence equations solved (k and ω). So the turbulent (RANS) length scale is a function of time as well as space. This feature facilitates the computation to be cognizant of the eddy length scales and hence behave as RANS or LES depending on the instantaneous local conditions, unlike in the case of a Spalart–Allmaras based DES, where DES acts just like a wall model. Another prominent feature of the DES version of the SST model is that although an instantaneous discontinuity may exist between the RANS region and the LES region, in the mean however a smooth transition takes place from RANS to LES and vice versa. It can be observed from Fig. 4 that the RANS regions transition into LES smoothly. In a DES Spalart–Allmaras model, the distance from the wall determines the switch from RANS to LES, which is not as receptive to instantaneous flow features.

The near wall region is always resolved in the RANS mode which transitions to the LES mode as the distance from the wall increases. The flow in the vicinity of the ribs is mostly resolved in LES mode all the way to the channel center. This includes the unsteady large-scale dynamics of the separated shear layer as shown in Fig. 4(b). In the inter-rib spacing, LES is only active near the ribbed wall and transitions to a full RANS mode at the center of the channel.

The grid facilitates the computation of the region in RANS and/or LES depending on the instantaneous conditions existing in the region. Downstream of the rib in

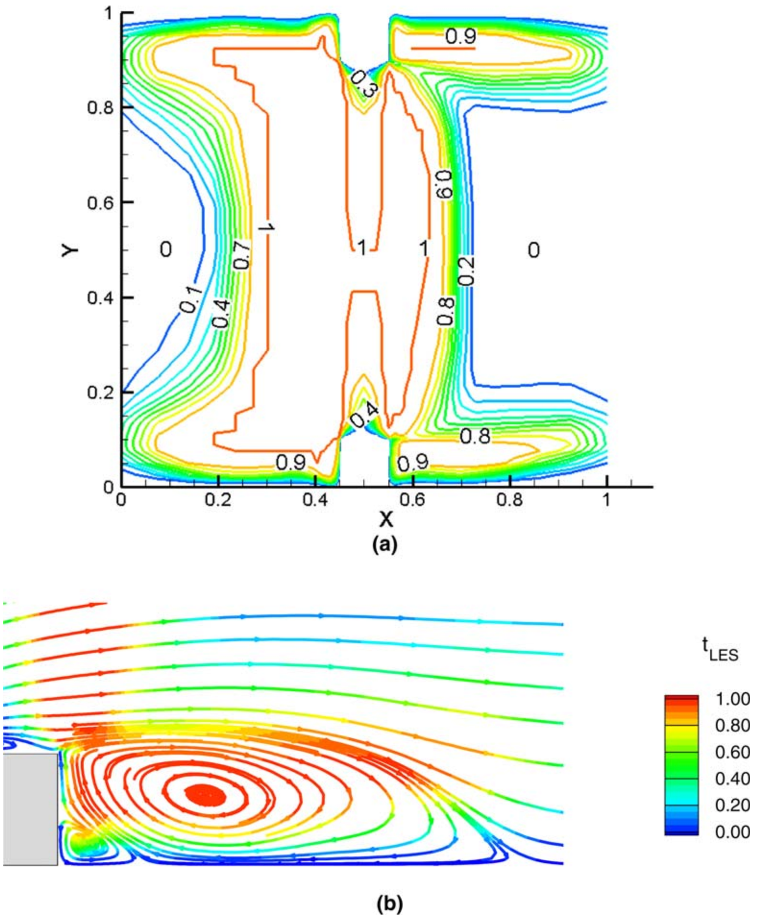

Fig. 4. (a) Plot of the DES regions in the center plane ($z/D_h = 0.5$) of the duct. A value $t_{LES} = 0$ denotes a region completely solved in URANS mode while $t_{LES} = 1$ denotes a complete LES mode. (b) Streamlines showing the DES regions in the recirculation region. A major part of the recirculation region is solved in the LES mode.

the region of separation (Fig. 4(b)) it is observed that the computation is mostly carried out in the LES mode which ensures that the unsteady physics in the separated region is captured accurately. Regions of low turbulence in between the ribs are completely solved in RANS mode.

7.3. Mean flow field

Early studies in turbulent channel flow (Halleen and Johnston, 1967; Lezius and Johnston, 1976) have established two important effects of rotation. When the rotational axis is perpendicular to the plane of mean shear, Coriolis forces have a considerable effect on the mean flow as well as on turbulent fluctuations. These effects are manifested as stabilization/destabilization of turbulence at leading/trailing walls and the generation of spanwise roll cells or secondary flow patterns. The secondary flow patterns are a direct result of the action of Coriolis forces on mean shear and are also observed in laminar flows subjected to system rotation.

It is well established that the production of turbulence in the near wall region and in shear layers is caused by the exchange of momentum through intense interactions between the fluctuating streamwise and cross-stream velocities. When Coriolis forces act in tandem with these events, turbulence is augmented, whereas it is attenuated when the two act in opposition. In the ribbed duct flow in this study, both the turbulent shear layer and near wall turbulence on the trailing surface are augmented by the direct effect of Coriolis forces, while the opposite effect comes into play at the leading wall. The results for all three rotation numbers follow the general trends outlined above.

The flow at the center ($z = 0.5$) of the duct is characterized by a large primary recirculation region behind the rib, a small secondary eddy trapped between the primary recirculation zone and the rib, a region of recirculation in front of the rib, and a small eddy on top of the rib. For a non-rotating case all these features are similar on both the ribbed walls. The reattachment of the rib separated shear layer was observed to be in the range 4.0–4.25e for the non-rotating case (Rau et al., 1988). The reattachment length predicted by DES was 4.1e which matched quite well with the experiments and LES predictions.

Fig. 5 shows the streamlines at the center of the duct ($z = 0.5$) for the three rotation cases. Rotational Coriolis forces affect the size of the recirculation zones and so the flow is asymmetric about the center y-plane of the duct. The reattachment length increases at the leading wall and decreases at the trailing wall with rotation number. The reattachment is observed at around 4.0e for $Ro = 0.18$ at the trailing side. The size of the separation bubble decreases to a value close to 3.6e when the rotation increases to 0.35. On increasing the rotation further to 0.67 the reattachment length remains almost the same as the 0.35 case. On the other hand, the reattachment length at the leading wall increases from a value of 4.0–4.25e for the stationary case ($Ro = 0.0$) to a value of 4.5e at $Ro = 0.18$. No significant change is observed as the Ro is increased to 0.36, but on increasing the rotation further to 0.67, the recirculation region is observed to increase to a value of around 6.7e, and as a result it merges with the recirculation region in front of the next rib.

The reattachment lengths for the rotating cases are consistent with the LES predictions (Abdel-Wahab and Tafti, 2004a,b). Fig. 6 shows the comparison of the flowfield as predicted by LES, DES and URANS. The separation and reattachment downstream of the rib is predicted accurately by DES and the reattachment length is in agreement with LES both at the leading and the trailing walls. However URANS overpredicts the reattachment lengths both at the leading as well as the trailing wall. Overprediction of the reattachment lengths is a result of the inability of the SST model to account for the effects of Coriolis forces, whereas in DES, the effect of Coriolis forces is captured in the resolved scales.

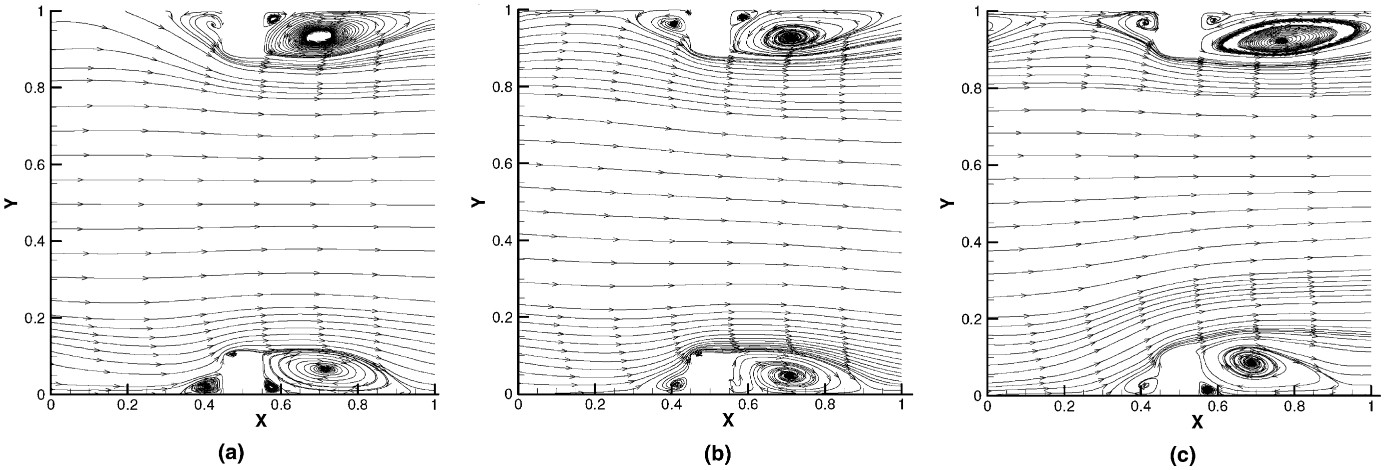

(a) (b) (c)

Fig. 5. Streamlines showing the flow in a fully developed duct as predicted by DES SST at $Z = 0.5$. $Ro = 0.18$ (a); 0.35 (b); 0.67 (c). $Y = 0$ represents the trailing wall, while $Y = 1$ represents the leading wall. Flow direction is from left to right.

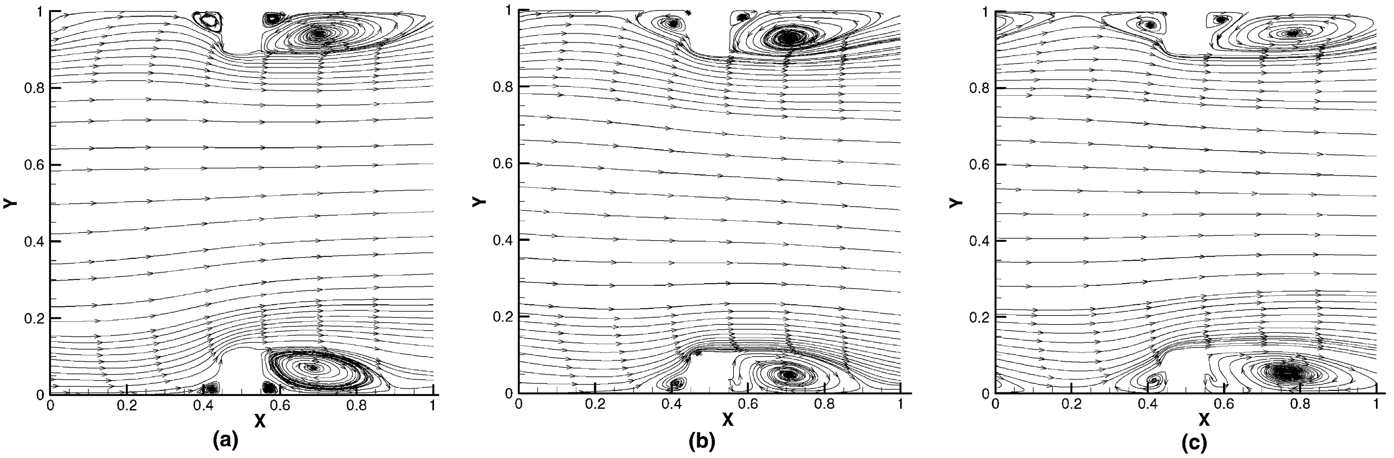

Fig. 6. Streamlines showing the flow in a fully developed duct rotating at $Ro = 0.35$ at $Z = 0.5$ as predicted by (a) LES; (b) DES SST; (c) URANS SST. $Y = 0$ represents the trailing wall, while $Y = 1$ represents the leading wall. Flow direction is from left to right.

The secondary flow in between the two ribs (Fig. 7) shows the presence of a pair of corner vortices in each quadrant when the ribbed duct is stationary. Similar vortices were observed by Liou et al. (2001) in their experiments. As the rotation increases to $Ro = 0.18$, the vortices on the leading side disappear, while the vortices at the trailing wall grow and move towards the center of the duct. As the rotation increases further the two vortices merge and grow bigger. At $Ro = 0.67$, the vortices occupy almost 80% of the channel height as observed in Fig. 7(d).

While Fig. 7 shows the structure of the secondary flow, Fig. 8 shows the magnitude of the secondary flows (v, w velocities) for the stationary and the three rotation cases in the cross-section of the duct on top of the rib. The v- and w-velocities are plotted individually in each half of the span. Above the rib, the constriction posed by the rib results in flow being pushed towards the channel center, both at the center of the span and near the side wall. In addition to this effect, a spanwise flow is setup toward the center and toward the side wall which is represented by the high positive impingement w-velocities at the side wall. As rotation increases, the strength of the secondary impingement flow at the trailing side increases while it decreases at the leading side, which is evident from the intrusion of the high v-velocities towards the leading side near the side wall. The asymmetry in the w-velocity also increases as the rotation increases.

7.4. Turbulent flow characteristics

A comparison of the instantaneous coherent vorticity (Joeng and Hussain, 1995) as predicted by 128^3 LES, 64^3 DES and 64^3 URANS is shown in Fig. 9. These plots give an idea of the flow structures resolved by the three schemes. It is observed that the magnitude of coherent vorticity and the flow characteristics predicted by DES is consistent with the magnitudes predicted by LES on a much finer grid. Predictions by URANS show lower vorticity levels as compared to LES and DES, both in the center of the duct as well as the inter-rib region. Thus the small modification in the length scales in the URANS model, which converts it into an equivalent DES model, substantially improves the fidelity of the simulation.

A comparison of the turbulent kinetic energies (TKE) predicted by the DES, LES and the URANS schemes are shown in Fig. 10. It is observed that the resolved component of TKE is significantly larger than the modeled component in the DES computation almost in the entire flow field. So the resolved component of TKE is considered for comparison for the DES and the LES cases, while the sum of the resolved and modeled components are considered for the URANS case.[3] A comparison of the TKE on top of the rib shows that the values resolved by DES compare well with that resolved by LES for all the three rotation cases. Localized peaks are observed at the trailing wall and the leading wall corresponding to the shear layer on top of the rib. The peak TKE at the trailing wall is around 0.28 for $Ro = 0.18$. The value is almost constant as the rotation increases to a value of 0.35 but shows a dramatic increase as the Ro increases further to 0.67 where the peak is around 0.38. At the leading wall the peak TKE reduces from a value of about 0.2 for the lowest rotation case to about 0.15 for the highest rotation case. The trend predicted by URANS at low rotation partly agrees with the LES computations towards the center of the channel, but the peaks in the shear layer are underpredicted by nearly 50%. At higher rotation cases the TKE are underpredicted through the complete height of the duct.

TKE values in between the ribs show similar trends. The location is just downstream of the reattachment point at

---

[3] For DES, the magnitude of the modeled stresses vary from values $< 10^{-1}$% on top of the ribs where the grid is fine to around 2% near the periodic face where the grid density is coarser. For URANS, the magnitude of the modeled stresses is as high as the resolved component in some regions of the flow.

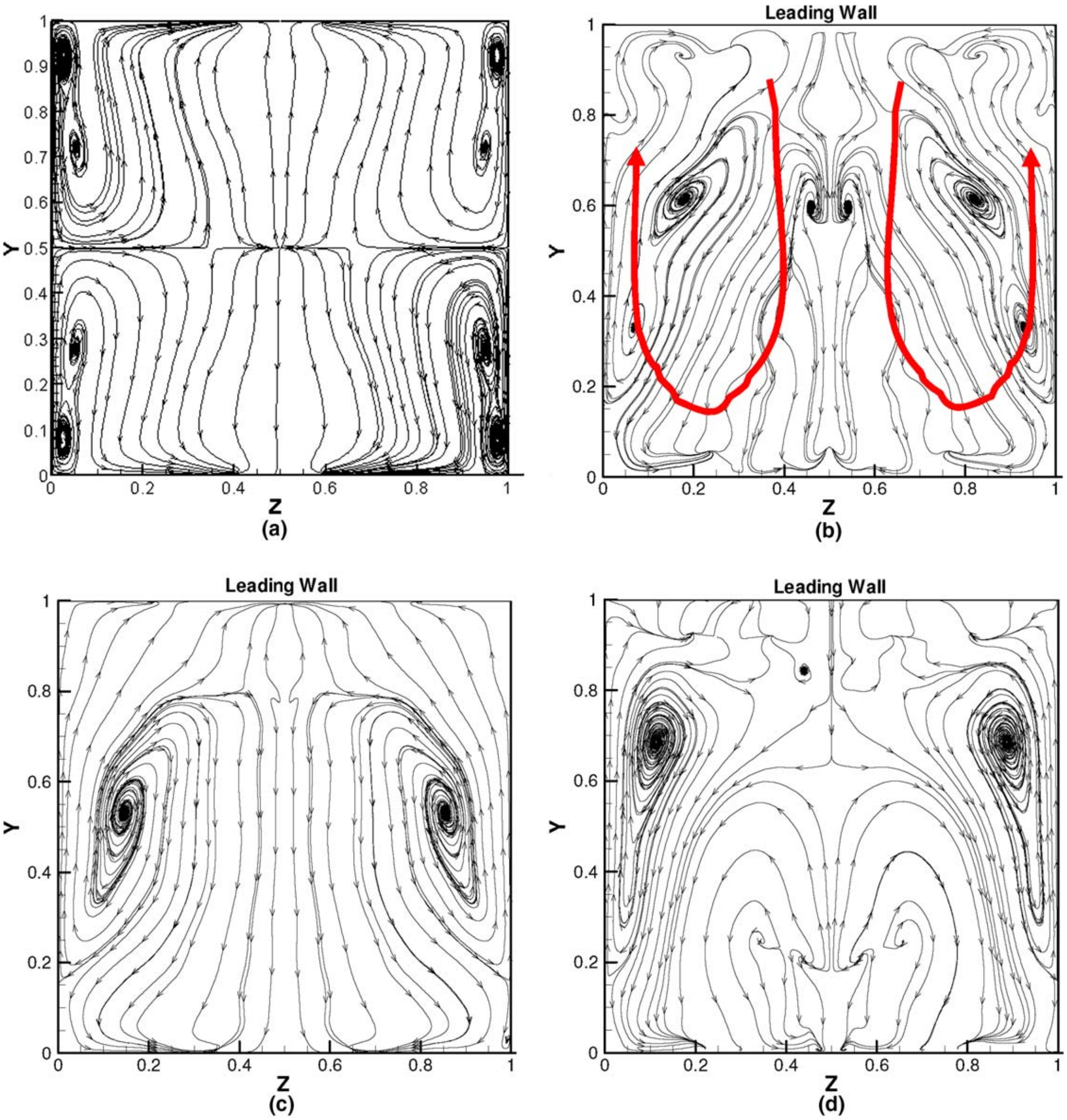

Fig. 7. Streamlines showing the secondary flow in the center of the inter-rib space for $Ro = 0.0$ (a); 0.18 (b); 0.35 (c); 0.67 (d) as predicted by DES SST: Arrows emphasis the direction of the secondary flow.

the trailing wall and so represents the region of boundary layer redevelopment in all the three rotation cases. It is observed that DES underpredicts the TKE values in the boundary layer as compared to LES, but shear layer turbulence away from the immediate vicinity of the wall is represented accurately in all the cases. On the other hand, URANS drastically underpredicts the TKE values in all three rotation cases. The low turbulence levels in URANS results in larger recirculation regions as compared to DES and LES.

Fig. 11 shows the power spectral density of the instantaneous streamwise velocity, obtained using a fast Fourier transform in the frequency domain for $Ro = 0.35$ at the leading wall of the duct. The most energetic mode is found at a non-dimensional frequency of approximately 11. The inset in the figure shows the spectral density obtained using Welch's averaged, modified periodogram method using MATLAB's *psd* function (MATLAB, 2005). Welch's method is a modified periodogram which divides the time signal into windows or blocks, computes the FFT for each individual window and averages to obtain the discrete Fourier transforms for the whole time signal considered. Welch's method tends to average out the peaks observed in a plain FFT and gives a single characteristic non-dimensional frequency of 35. In the following figures, the smoothed spectral density is used to compare the energy carried by the resolved scales.

Figs. 12 and 13 show the turbulent spectrum and the sampled signal at the leading and trailing walls. Data was collected by placing probes in the shear layer near the reattachment region. Three probes were placed at the leading and the trailing walls in regions where the computation is completely RANS ($t_{\mathrm{LES}} = 0.0$), partially RANS and partially LES ($t_{\mathrm{LES}} = 0.5$) and completely LES ($t_{\mathrm{LES}} = 1.0$).

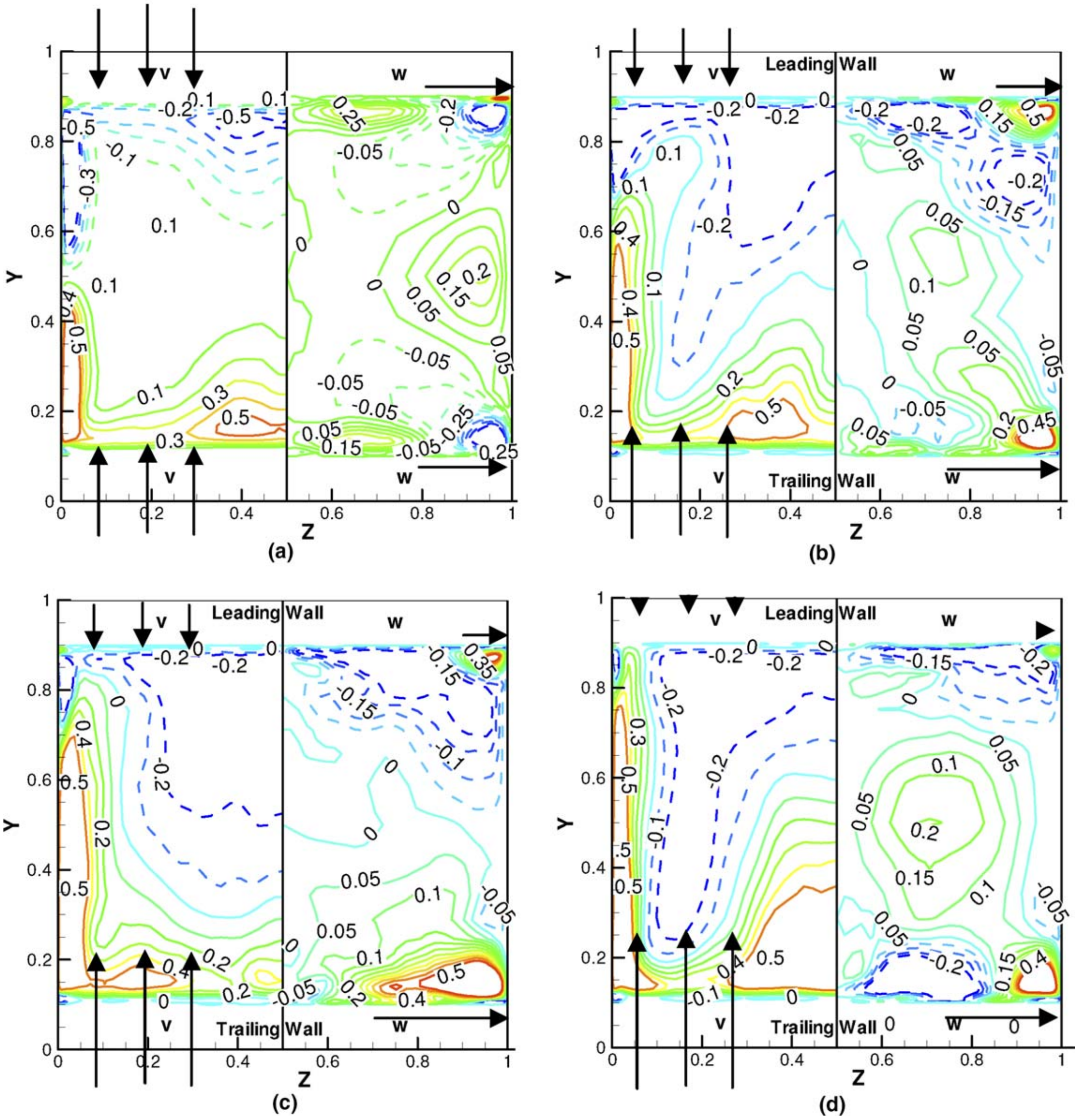

Fig. 8. Secondary flow contours on the rib for $Ro = 0.0$ (a); 0.18 (b); 0.35 (c); 0.67 (d) as predicted by DES SST. The contours show the effect of rotation on the secondary flow in the cross-section. The arrows qualitatively represent the effect of rotation on the magnitude of the v- and w-velocities.

From the signals it is observed that the DES computation shows more unsteadiness, hence more resolved energy, as compared to the URANS computation. A one to one comparison can be made at the location at which $t_{\mathrm{LES}} = 0.0$ (full URANS in DES approach) versus the same location in the URANS calculation in Figs. 12 and 13. At the leading wall the resolved peak energy between the two cases varies by nearly two orders of magnitude, whereas at the trailing wall the ratio is about 5. Larger differences between DES and URANS is found at locations where DES operates in full LES mode ($t_{\mathrm{LES}} = 1.0$). Comparison of LES with DES at locations where $t_{\mathrm{LES}} = 1.0$ (full LES mode) shows that the peak resolved energy is of comparable magnitude – at the trailing wall, the LES peak is at 4 whereas the DES peaks at 4.5. At the leading wall, the DES peak energy is higher at 1.5 than the corresponding LES, which is at 0.6, indicating that the level of turbulent fluctuations is higher at this location in the DES calculation. This is suspected to be caused by a slight shift in the shear layer trajectory.

Figs. 12 and 13 bring out an important observation, that for the same resolution, the DES framework allows a much larger part of the energy spectrum or scales to be resolved on the grid. While URANS picks up the most energetic modes, only a fraction of the energy is present in the grid scales. This would not be a problem if the models were true to the physics, which for rotating ducts is not the case. The SST model does not include the effect of Coriolis forces on turbulence, but the consequence of that shortcoming is felt much more in the URANS model than in DES because a large fraction of the modal energy is resolved on the grid by DES and the effect of Coriolis forces is included directly through the momentum equations.

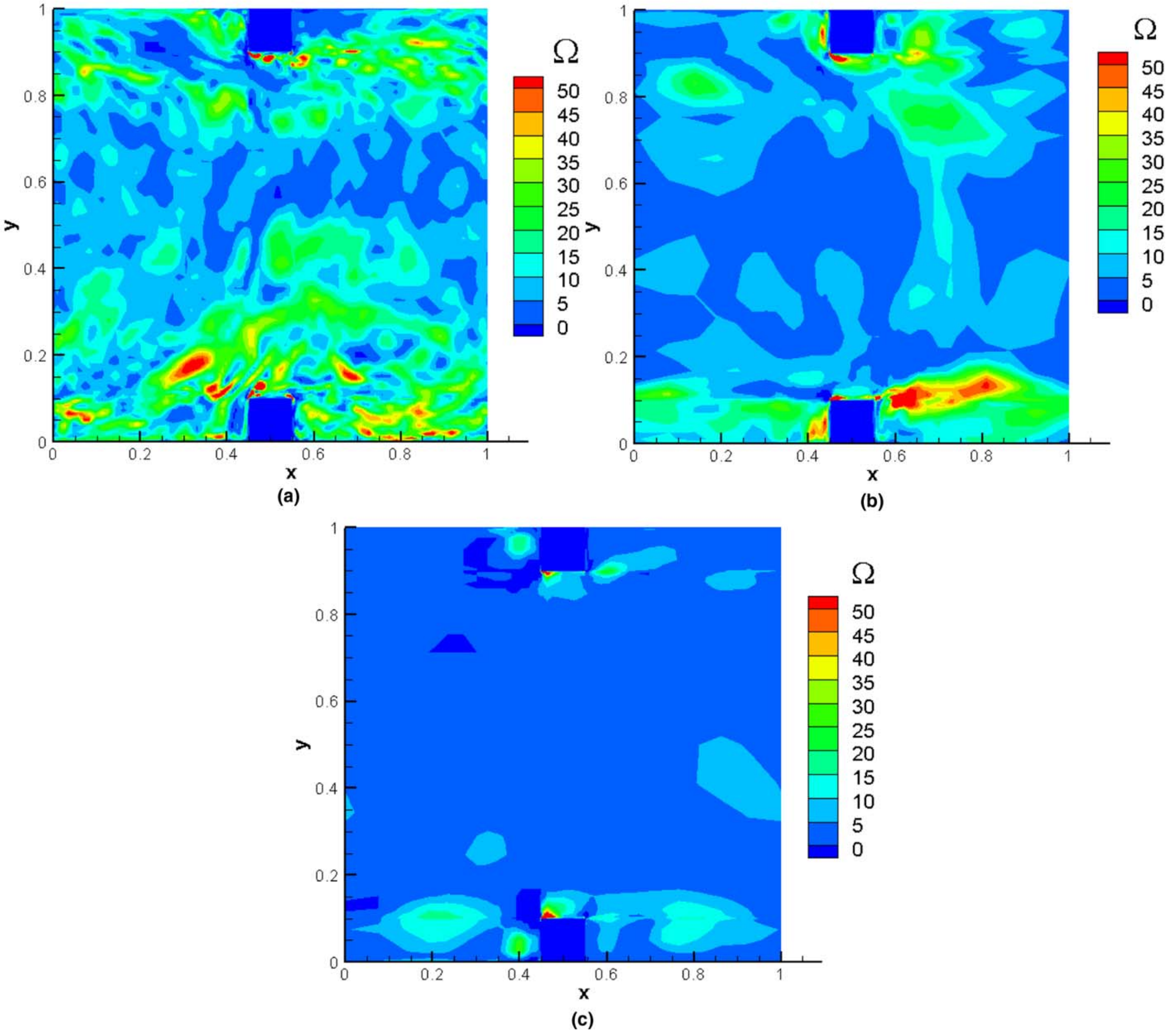

Fig. 9. Coherent vorticity contours for the (a) LES 128^3; (b) DES 64^3; (c) URANS 64^3 for $Ro = 0.35$ show the scales resolved of the three schemes at $z = 0.5$.

7.5. Mean heat transfer

The heat transfer trends at the leading and trailing walls are similar to the trends observed at the ribbed walls for the stationary case. The augmentation ratio is high in front of the rib as a result of the unsteady vortices in this region. These secondary vortices continuously transport cooler fluid from the mainstream to the ribbed wall increasing the heat transfer coefficient. Immediately behind the rib, a secondary recirculation is trapped between the wall and the primary recirculation zone. Although the action of the secondary eddy causes some localized augmentation in this region, the overall augmentation is low and similar to that in a smooth duct. Further downstream, the heat transfer coefficient increases steadily as the vortices from the separated shear layer impinge on the wall.

Fig. 14 shows the heat transfer at the leading (upper half) and the trailing walls (lower half) for the three rotation cases. As the rotation number is increased, an increase in the heat transfer is observed at the trailing wall, especially in regions immediately upstream of the rib and near the reattachment point. This is countered by a decrease at the leading wall in the corresponding regions. The heat transfer augmentation in the region upstream of the reattachment point at the trailing wall increases from 4.4 for $Ro = 0.18$ to 4.8 for $Ro = 0.35$ and 5.6–6.0 for $Ro = 0.67$. At the leading wall the heat transfer upstream of the reattachment point is observed to decrease from 2.8 for $Ro = 0.18$ to 1.6 for $Ro = 0.35$ and 0.67 respectively.

Fig. 15 shows a comparison of the DES and the URANS with LES results at $Ro = 0.35$. This shows that the URANS under-predicts the heat transfer at the trailing

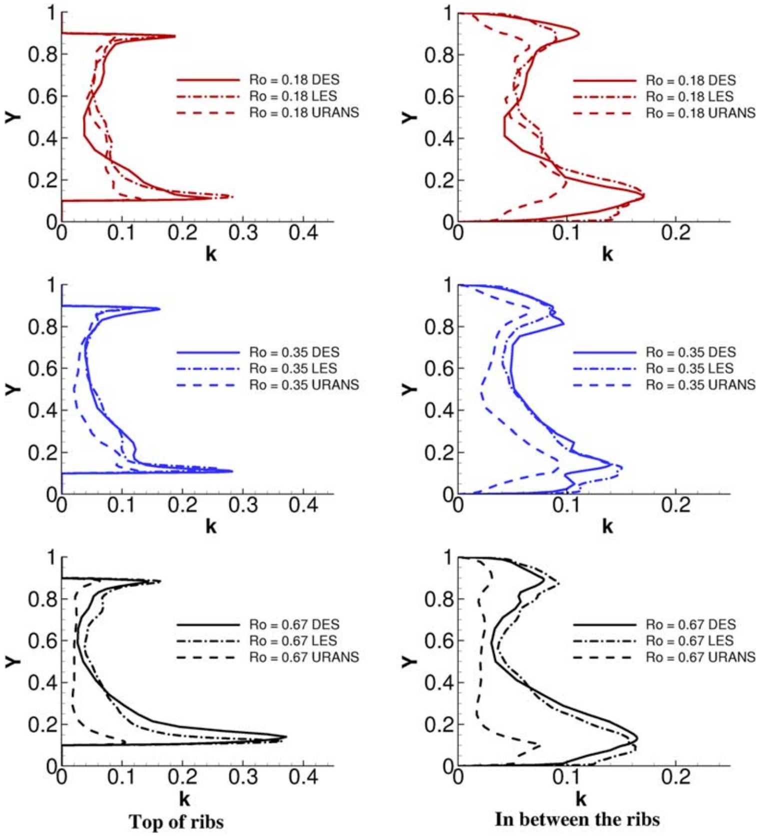

Fig. 10. TKE values as predicted by the DES, LES and the URANS cases for the three rotation cases on top of the ribs and in between the ribs.

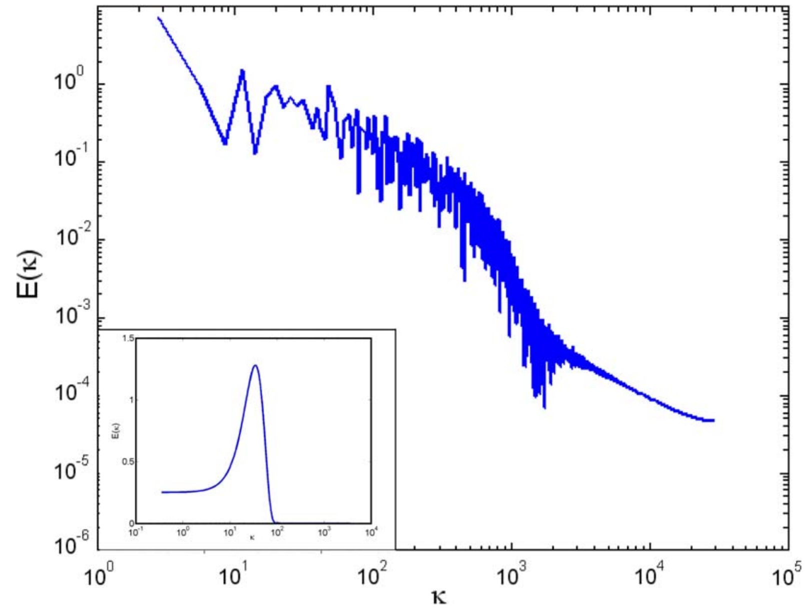

Fig. 11. Power spectral density at the leading wall for $Ro = 0.35$ with DES. The inset shows the equivalent semi-log scale representation, which is used to compare the relative magnitudes of the dominant frequency in Figs. 12 and 13.

side, where the turbulence is enhanced by rotation. The heat transfer augmentation predicted by DES agrees quite well with the LES computations. The peak heat transfer on the trailing wall in the region of shear layer reattachment is shifted away from the center of the duct due to the effect of secondary flows and is captured by all three methods. However, the URANS predicts this region further downstream because of the larger reattachment length. Heat

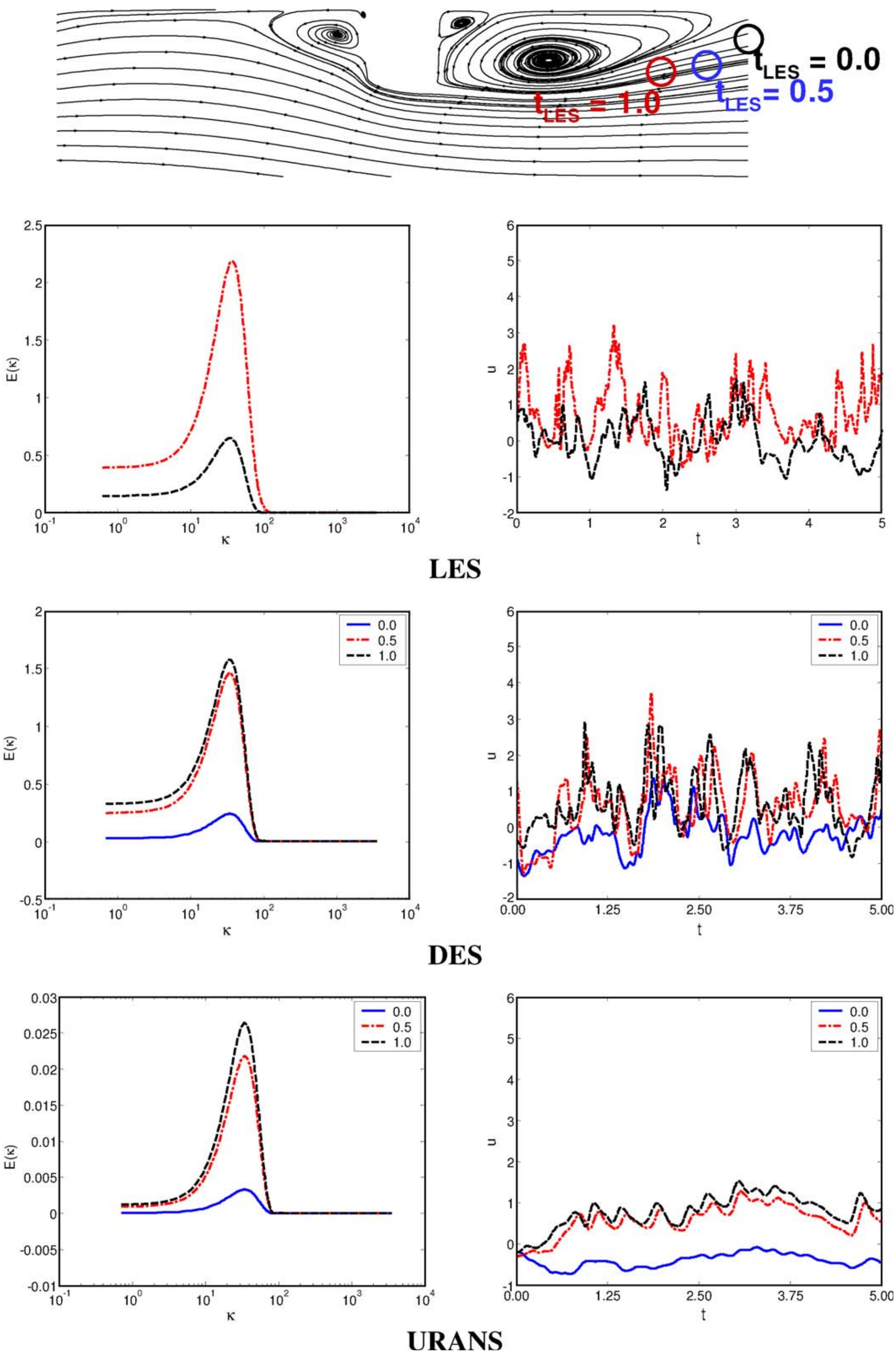

Fig. 12. Turbulence spectrum and the signal sampled for 5.0 non-dimensional time units at the leading wall for $Ro = 0.35$.

transfer augmentations at the trailing wall reach values close to 5.2 immediately upstream of the rib where the unsteady vortices enhance the heat transfer. Both DES and URANS tend to over-predict the spatial extent of this region.

The flow at the leading wall is more stable than the flow at the trailing wall and so the overall heat transfer at the leading wall is almost half the heat transfer at the trailing wall. Upstream of the rib, heat transfer levels are almost 2.8 times that observed in a smooth duct case. Once again,

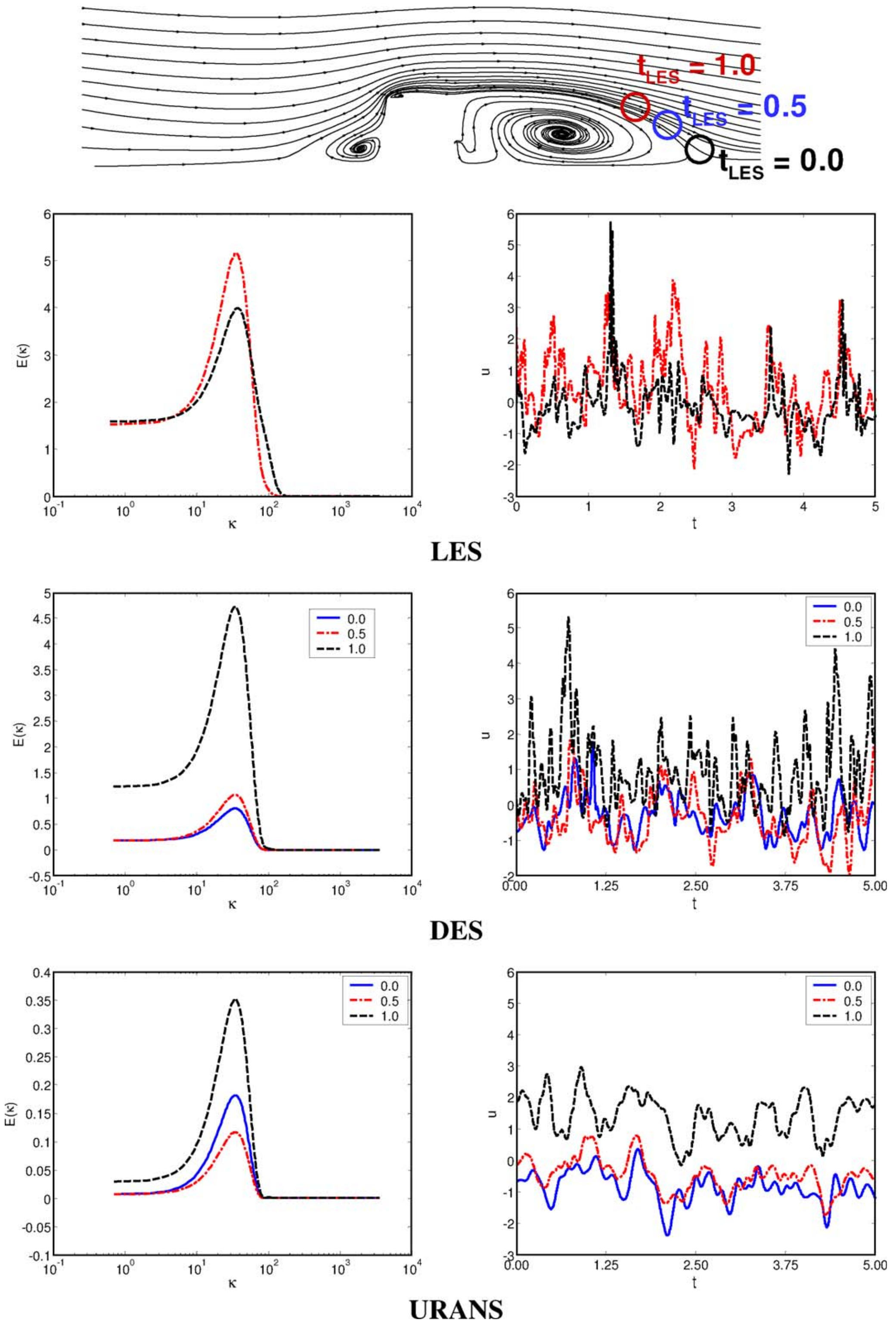

Fig. 13. Turbulence spectrum and the signal sampled for 5.0 non-dimensional time units at the trailing wall for $Ro = 0.35$.

both DES and URANS overpredict the extent and augmentation in this region. The heat transfer levels drop to values close to the smooth channel heat transfer values immediately behind the rib, but the augmentation increases to values close to 1.6 downstream of the reattachment point.

The trends predicted by DES are consistent with the LES results (Abdel-Wahab and Tafti, 2004a,b), with the exception of the region immediately upstream of the rib where higher levels of heat transfer are predicted. Similar results were observed by Viswanathan and Tafti (2004, 2005c) in a stationary duct where a larger heat transfer aug-

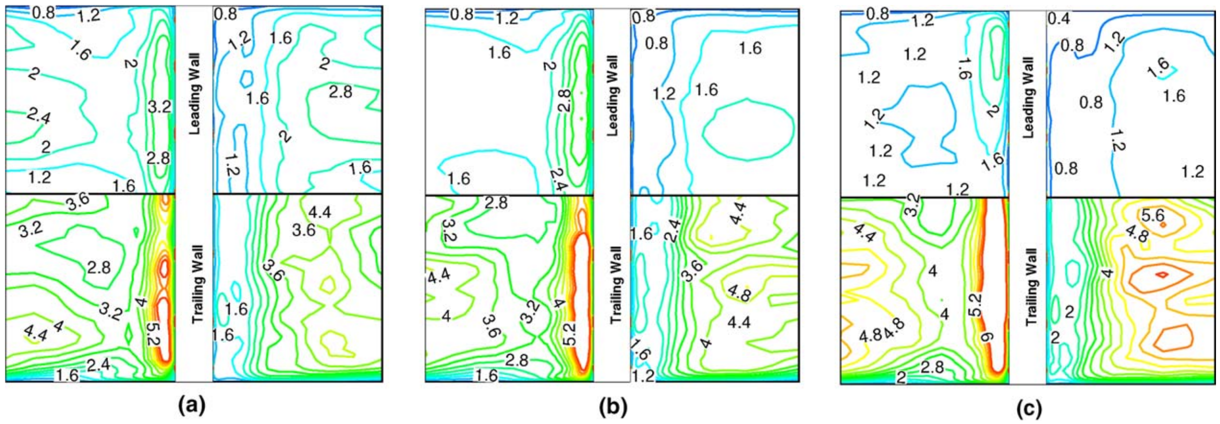

Fig. 14. Heat transfer augmentation (Nu/Nu_0) predicted at the leading and the trailing walls by DES SST for $Ro = 0.18$ (a); 0.35 (b); 0.67 (c). Flow direction is from left to right.

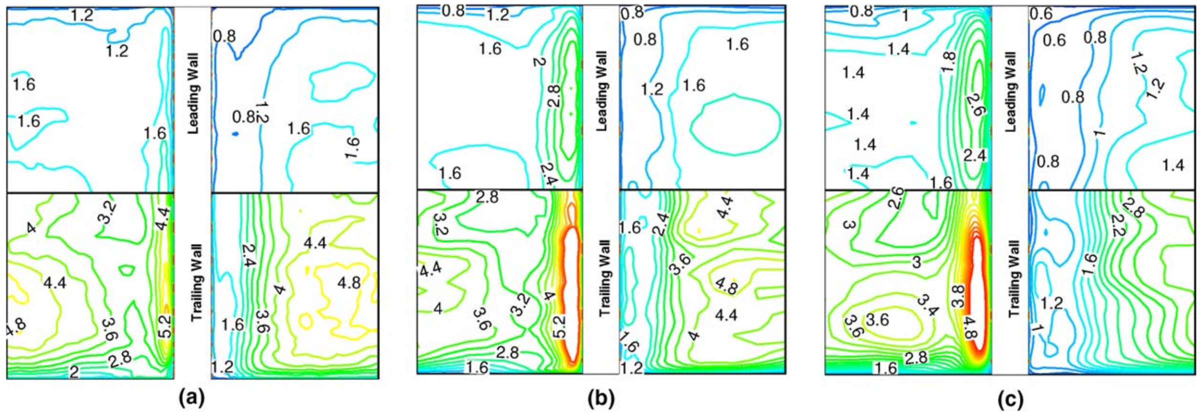

Fig. 15. Heat transfer augmentation (Nu/Nu_0) predicted at the leading and the trailing walls for the $Ro = 0.35$ case by (a) LES; (b) DES SST; (c) URANS SST. Flow direction is from left to right.

mentation was observed immediately upstream of the rib. On the other hand URANS results show a lot of discrepancy. The most prominent deviation from LES is the under-prediction of the heat transfer at the trailing wall of the duct. The heat transfer distributions at the ribbed walls are also much smoother than LES and DES predictions.

The secondary flows in the stationary and the rotation cases play a major role in the heat transfer at the side walls. Along the smooth (side) walls the heat transfer increases on moving from the trailing wall and reaches a maximum at the top front corner of the rib as a result of the secondary flow impingement on the wall. The heat transfer decreases on the side walls towards the center of the channel. Though the heat transfer patterns are the same for the stationary and the rotation cases the magnitudes of heat transfer are a function of the rotation.

For $Ro = 0.18$ (Fig. 16) the secondary flow impingement results in levels of heat transfer as high as seven times that in a smooth channel at the trailing wall, at the corner of the rib and the side wall. The heat transfer decreases to values close to 2.0 towards the center of the duct. On moving towards the leading wall the heat transfer decreases further and drops to values lower than unity near the leading wall of the side wall. However secondary flow impingement near the corner of the ribs locally results in higher heat transfer. As the rotation increases higher heat transfer is observed near trailing wall and lower hear transfer regions move closer to the leading wall. This behavior is consistent with the secondary flow features observed, i.e., stronger the impingement more is the heat transfer at the side walls.

Fig. 17 compares the side wall heat transfer predicted by DES and URANS with LES for $Ro = 0.35$. The DES predictions compare well with LES. URANS predicts comparable trends except that a noticeably larger augmentation region is predicted near the rib at the trailing wall and the augmentation ratio is also underpredicted at the center of the duct and in the vicinity of the trailing wall.

Fig. 18 shows a gradual increase in the average heat transfer augmentation at the side walls as the rotation number increases from 0 to 0.67. DES predicts these trends accurately but slightly underpredicts the augmentation compared to LES. URANS severely underpredicts the side wall heat transfer at $Ro = 0.18$ and 0.35, while the agreement is comparatively better at the highest rotation number.

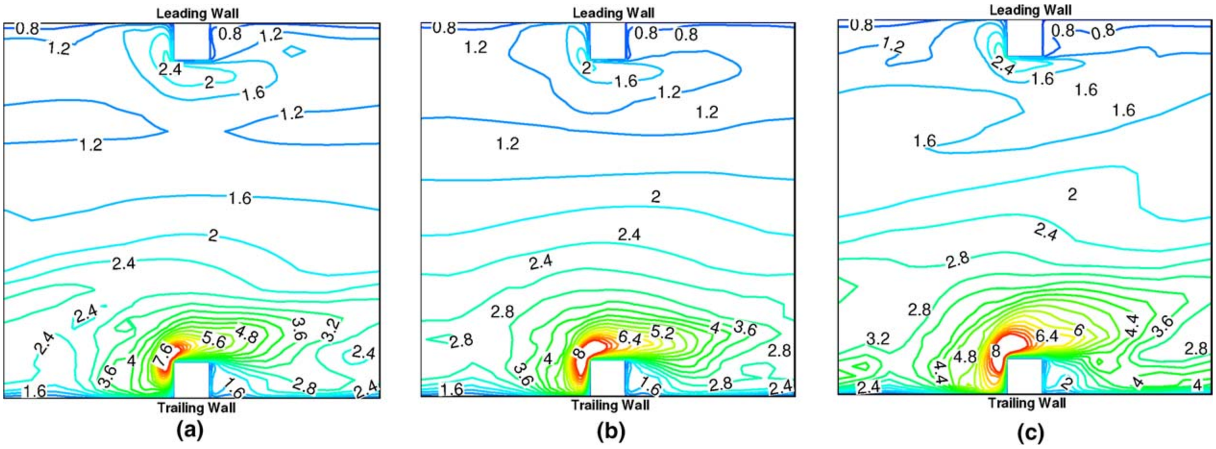

Fig. 16. Heat transfer augmentation (Nu/Nu_0) predicted at the side wall by DES SST for the $Ro = 0.18$ (a); 0.35 (b); 0.67 (c). Flow direction is from left to right.

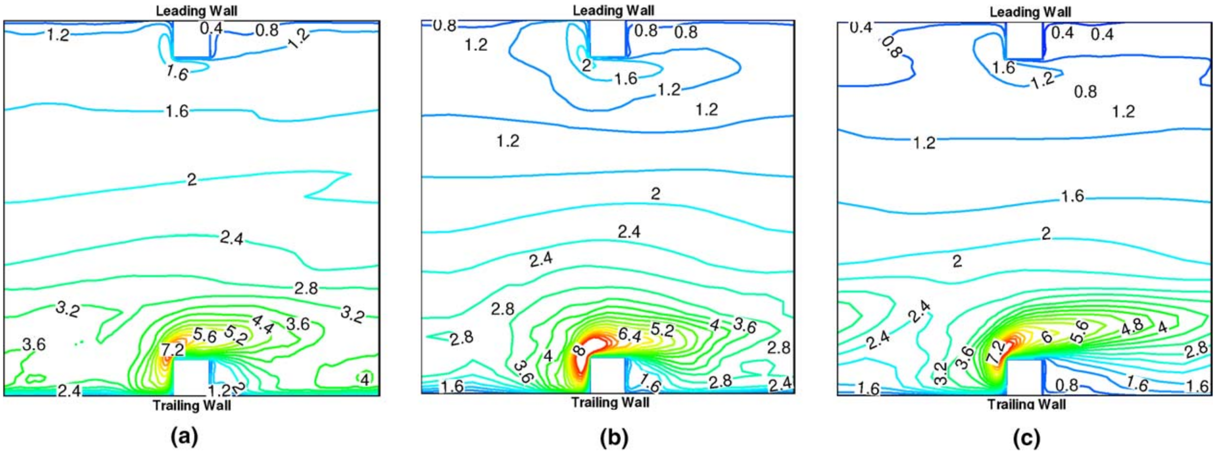

Fig. 17. Heat transfer augmentation (Nu/Nu_0) predicted at the side wall for the $Ro = 0.35$ case by (a) LES; (b) DES SST; (c) URANS SST. Flow direction is from left to right.

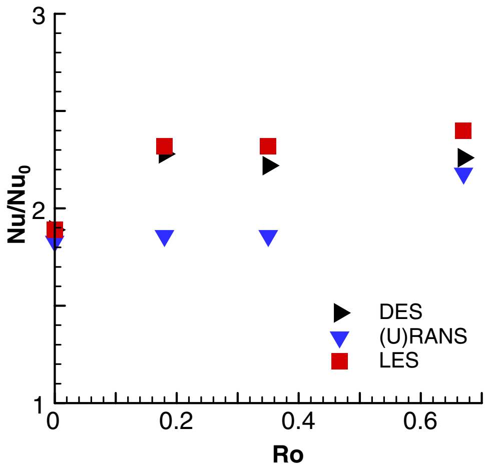

Fig. 18. Side wall heat transfer predicted by LES, DES and URANS for the various rotation cases.

The effect of rotation is more prominent at the leading and the trailing walls. Results for averaged Nusselt numbers on the leading and trailing faces for the three rotation numbers are compared with the experiments of Liou et al. (2001), Parsons et al. (1994), and Wagner et al. (1992). The experimental data of Liou et al. (2001) is at $Re = 10{,}000$ for $e/D_h = 0.136$ and $P/e = 10$ and Parsons et al. (1994) data is obtained at $Re = 5000$ for $e/D_h = 0.125$ and $P/e = 10$. The data of Wagner et al. (1992) includes the effects of buoyancy with a density ratio = 0.04 for a staggered rib arrangement with $e/D_h = 0.1$ and $P/e = 10$ at $Re = 25{,}000$. Wagner's data includes the effects of centrifugal buoyancy which increase trailing wall heat transfer as the rotation number increases. In all cases, fully developed data is extracted for comparison. Fig. 19 compares the overall heat transfer augmentations at the leading and trailing walls predicted by DES and URANS cases, with the LES computations and experimental results. DES predictions agree well with experiments and LES except for the trailing side at $Ro = 0.18$, where the augmentation is

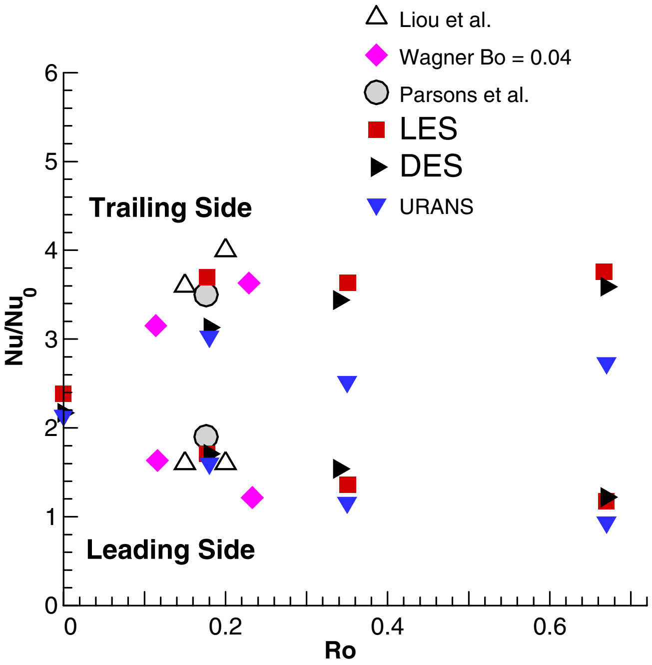

Fig. 19. Comparison of average Nusselt number augmentation ratios at the leading and trailing sides with experiments.

underpredicted by 11% compared to Parson's data and about 15% compared to LES. On the other hand, URANS substantially underpredicts the trailing wall augmentation, by as much as 30% compared to LES, at the high rotation numbers of 0.35 and 0.67. Prediction accuracy of URANS is similar to that of DES at the leading wall which is within 10% of LES.

8. Conclusions

Results from DES and URANS of a fully developed flow in a 90° ribbed duct are presented for three rotation cases – $Ro = 0.18$, 0.35 and 0.67 at a Reynolds number of 20,000. The computations were performed on a 64^3 mesh tested earlier for a stationary case which is almost an order of magnitude less expensive than the analogous LES computation on a 128^3 mesh (Abdel-Wahab and Tafti, 2004a,b).

The effect of rotation is observed by the increase in the unsteadiness at the trailing wall due to which the reattachment length decreases. Secondary flow impingement is observed to become stronger as rotation increases. These flow features result in an increase in the heat transfer at the trailing wall. The peak heat transfer level increases from a value of about 3.0 for the stationary duct to a value of about 6.0 for the largest rotation. The overall heat transfer at the trailing wall increases by almost a factor of 1.5 as the system is rotated from rest to $Ro = 0.67$.

At the leading wall the opposite effect is observed. Rotation damps turbulence at the leading wall resulting in larger recirculation regions. It is observed that the recirculation region downstream of the rib almost overlaps the recirculation region upstream of the next rib. This results in low levels of heat transfer at the leading wall. The heat transfer distribution drops to values close to that in a smooth duct for the highest rotation considered.

The heat transfer at the side walls show distributions similar to a stationary duct. The heat transfer is high at the corner of the rib, which is due to the impingement of the secondary flows on the side walls. The heat transfer decreases on moving from the trailing wall to the leading wall. Rotation increases the magnitude of the secondary flows and increases the heat transfer augmentation on the side walls.

The flow and heat transfer distribution predicted by the SST DES case is consistent with the LES predictions. Though higher heat transfer is predicted immediately upstream of the rib, the distribution in the other regions are accurate. The overall heat transfer predicted also match well with the LES predictions and the experimental observations. URANS fails to capture the effects of the Coriolis forces at the trailing walls and underpredicts the heat transfer.

In summary, it is concluded that DES accurately predicts the physics of the rotation dominated flow, in addition to accurately predicting separation and reattachment and unsteady vortex induced secondary motions. The main contribution of this paper is in establishing that DES, like LES, can produce good quality results at a much lower cost than an equivalent well-resolved LES. The payoffs of DES are expected to be more at higher Reynolds numbers.

References

Abdel-Wahab, S., Tafti, D.K., 2004a. Large eddy simulations of flow and heat transfer in a 90° ribbed duct with rotation – effect of Coriolis and centrifugal buoyancy forces. J. Turbomach. 126 (4), 627–636.

Abdel-Wahab, S., Tafti, D.K., 2004b. Large eddy simulations of flow and heat transfer in a 90° ribbed duct with rotation. Effect of coriolis forces, GT2004-53796, ASME Turbo Expo: 2004, Vienna, Austria.

Abdel-Wahab, S., Tafti, D.K., 2004c. Large eddy simulation of flow and heat transfer in a staggered 45° ribbed duct. Paper no. GT2004-53800, ASME Turbo Expo: 2004, Vienna, Austria, 14–17 June 2004.

Amano, R.S., Goel, P., 1995. Computation of turbulent flow beyond backward steps using Reynolds stress closure. AIAA J 23, 1356.

Bradshaw, P., 1969. The analogy between streamline curvature and buoyancy in turbulent shear flow. J. Fluid Mech. 36 (Part 1), 177–191.

Bradshaw, P., 1988. In: Kline, S.J., Afghan, N.H. (Eds.), Effects of Extra Strain – Review, Near Wall turbulence, Zoran Zaric Memorial Conference. Hemisphere Publishing Corporation, pp. 106–122.

Bo, T., Iacovides, H., Launder, B.E., 1995. Developing buoyancy-modified turbulent flow in ducts rotating in orthogonal mode. Trans. ASME 177, 474–484.

Chima, R.V., 1996. A k–ω turbulence model for quasi-three dimensional turbo machinery flows, AIAA 96-0258.

Driver, D., Seegmiller, H.L., 1985. Features of reattaching turbulent shear layer in divergent channel flow. AIAA J. 23, 162–171.

Forsythe, J.R., Squires, K.D., Wurtzler, K.E., Spalart, P.R., 2002. Detached-eddy simulation of fighter aircraft at high alpha, AIAA Paper 2002-0591.

Halleen, R.M., Johnston, J.P., 1967. The influence of rotation of flow in a long rectangular channel – an experimental study, Report MD-18, Thermosciences Division, Dept. of Mech. Eng., Stanford University.

Hanjalic, K., Launder, B.E., 1980. Sensitizing the dissipation equation to irrotational strains. ASME J. Fluids Eng. 102, 34.

Hellsten, A., 1998. Some improvements in Menter's k–ω SST turbulence model, AIAA 98-2554.

Howard, J.H.G., Patankar, S.V., Bordynuik, R.M., 1980. Flow prediction in rotating ducts using Coriolis-modified turbulence models. ASME J. Fluids Eng. 102, 456–461.

Iacovides, H., Launder, B.E., 1991. Parametric and numerical study of fully developed flow and heat transfer in rotating rectangular ducts. J. Turbomach. 133, 331–338.

Incropera, F.P., Dewitt, D.P., 2002. Fundamentals of Heat and Mass Transfer, fifth ed. John Wiley and Sons, New York.

Ishigaki, H., 1996. Analogy between turbulence flows in curved pipes and orthogonally rotating pipes. J. Fluid Mech. 307, 1–10.

Joeng, J., Hussain, F., 1995. On the identification of a vortex. J. Fluid Mech. 285, 69–94.

Kapadia, S., Roy, S., Wurtlzer, K., 2003. Detached eddy simulation over a reference Ahmed car model, AIAA 2003-0857.

Launder, B.E., Priddin, C.H., Sharma, B.I., 1977. The calculation of turbulent boundary layers on spinning and curved surfaces. ASME J. Fluids Eng. (March), 231–239.

Lezius, D.K., Johnston, J.P., 1976. Roll-cell instabilities in rotating laminar and turbulent channel flows. J. Fluid Mech. 77 (Part 1), 153–175.

Lin, Y.L., Shih, T.I.-P., Stephens, M.A., Chyu, M.K., 2001. A numerical study of flow and heat transfer in a smooth and a ribbed U-duct with and without rotation. ASME J. Heat Transfer 123, 219–232.

Liou, T.M., Chen, M.Y., Tsai, M.H., 2001. Fluid flow and heat transfer in a rotating two-pass square duct with in-line 90° ribs, ASME Turbo Expo: 2001-GT-0185.

MATLAB, 2005. Release Notes for Release 14 with Service Pack 3.

Menter, F.R., 1992. Improved two-equation k–ω turbulence models for aerodynamic flows, NASA Technical Memorandum 103975.

Menter, F.R., 1993. Zonal two equation k–ω turbulence models for aerodynamic flows, AIAA Paper 93-2906.

Murata, A., Mochizuki, S., 1999. Effect of cross-sectional aspect ratio on turbulent heat transfer in an orthogonally rotating rectangular smooth duct. Int. J. Heat Mass Transfer 42, 3803–3814.

Murata, A., Mochizuki, S., 2000. Large eddy simulation with a dynamic subgrid-scale model of turbulent heat transfer in an orthogonally rotating rectangular duct with transverse rib turbulators. Int. J. Heat Mass Transfer 43, 1243–1259.

Nikitin, N.V., Nicoud, F., Wasistho, B., Squires, K.D., Spalart, P.R., 2000. An approach to wall modeling in large-eddy simulations. Phys. Fluids 12 (7), 1629–1632.

Parsons, J.A., Han, J.C., Zang, Y.M., 1994. Wall heating effect on local heat transfer in a rotating two-pass square channel with 90° rib turbulators. Int. J. Heat Mass Transfer 37, 1411–1420.

Prakash, C., Zerkle, R., 1995. Prediction of turbulent flow and heat transfer in a ribbed rectangular duct with and without rotation. J. Turbomach. 117, 255–264.

Rau, G., Cakan, M., Moeller, D., Arts, T., 1988. The effect of periodic ribs on local aerodynamic and heat transfer performance of a straight cooling channel. ASME J. Turbomach. 120, 368–375.

Rigby, D.L., 1998. Prediction of heat and mass transfer in a rotating ribbed coolant passage with a 180 degree turn, 98-GT-329, International Gas Turbine and Aeroengine Congress and Exhibition, Stockholm, Sweden, 2–5 June.

Rodi, W., Scheuerer, G., 1983. Calculation of curved shear layers with two-equation turbulence models. Phys. Fluids 26 (6).

Schweighofer, J., Hellsten, A., 1999. Computations of viscous flow around the HSVA-1 tanker using two versions of k–ω turbulence model. Helsinki University of Technology, Laboratory of Aerodynamics, Report B-51.

Sewall, E.A., Tafti, D.K., 2004a. Large eddy simulation of the developing region of a stationary ribbed internal turbine blade cooling channel, Paper no. GT2004-53832, ASME Turbo Expo: 2004, Vienna, Austria, 14–17 June 2004.

Sewall, E.A., Tafti, D.K., 2004b. Large eddy simulations of the developing region of a rotating ribbed internal turbine blade cooling channel, Paper no. GT2004-53833, ASME Turbo Expo: 2004, Vienna, Austria, 14–17 June 2004.

Sewall, E.A., Tafti, D.K., 2006. Large eddy simulation of flow and heat transfer in the 180° bend region of a stationary ribbed gas turbine internal cooling duct. J. Turbomach. 128.

Sewall, E.A., Tafti, D.K. Large eddy simulation of flow and heat transfer in the developing region of a rotating gas turbine blade internal cooling duct with coriolis forces and buoyancy forces, GT 2005-68519, ASME Turbo Expo 2005, Reno, J. Turbomach., accepted for publication.

Sewall, E.A., Tafti, D.K., Graham, A., Thole, K.A., 2006. Experimental validation of large eddy simulation of flow and heat transfer in a stationary ribbed duct. Int. J. Heat Fluid Flow 27 (2), 243–258.

Spalart, P.R., Jou, W.H., Streletes, M., Allmaras, S.R., 1997. Comments on the feasibility of LES for wings and a hybrid RANS/LES approach. In: Liu, C., Liu, Z. (Eds.), First AFSOR Int. Conf. on DNS/LES, 4–8 August 1997, Advances in DNS/LES. Greyden Press, Columbus, OH.

Speziale, G., Ngo, T., 1988. Numerical solution of turbulent flow past a backward-facing step using a nonlinear k–ε model. Int. J. Eng. Sci. 26, 1099–1112.

Squires, K.D., Forsythe, J.R., Morton, S.A., Blake, D.C., Serrano, M., Wurtzler, K.E., Strang, W.Z., Tomaro, R.F., Spalart, P.R., 2002. Analysis of full aircraft with massive separation using detached-eddy simulation. In: Proceedings of the High Performance Computing Modernization Program 2002 Users Group Conference, Austin, Texas.

Stephens, M.A., Shih, T.I.-P., Civinskous, K.C., 1996. Computations of flow and heat transfer in a rotating U-shaped square duct with smooth walls, AIAA 96-3161.

Strelets, M., 2001. Detached eddy simulation of massively separated flows, AIAA 2001-0879.

Tafti, D.K., 2001. GenIDLEST – A scalable parallel computational tool for simulating complex turbulent flowsProc. ASME Fluids Engineering Division, FED, vol. 256. ASME-IMECE, New York.

Tafti, D.K., 2005. Evaluating the role of subgrid stress modelling in a ribbed duct for the internal cooling of turbine blades. Int J Heat Fluid Flow 26 (1), 92–104.

Viswanathan, A.K., Tafti, D.K., 2004. Detached eddy simulation of turbulent flow and heat transfer in a duct, HT-FED2004-56152, 2004 ASME Heat Transfer/Fluids Engineering Summer Conference, Charlotte, 11–15 July.

Viswanathan, A.K., Tafti, D.K., 2005a. Detached eddy simulation of flow and heat transfer in a stationary internal cooling duct with skewed ribs, GT 2005-68118, ASME Turbo Expo: 2005, Reno-Tahoe, Nevada, USA, 6–9 June 2005.

Viswanathan, A.K., Tafti, D.K., 2005b. Large eddy simulation in a duct with rounded skewed ribs, GT 2005-68117, ASME Turbo Expo: 2005, Reno-Tahoe, Nevada, USA, 6–9 June 2005.

Viswanathan, A.K., Tafti, D.K., 2005c. Detached eddy simulation of turbulent flow and heat transfer in a duct. J. Fluids Eng. 127, 888–896.

Viswanathan, A.K., Tafti, D.K., 2006. Detached eddy simulation of turbulent flow and heat transfer in a two-pass internal cooling duct. Int. J Heat Fluid Flow 27 (1), 1–20.

Viswanathan, A.K., Tafti, D.K., Abdel-Wahab, S., 2005. Large eddy simulation of flow and heat transfer in an internal cooling duct with high-blockage 45° staggered ribs, GT 2005-68086, ASME Turbo Expo 2005, Reno-Tahoe, Nevada, USA, 6–9 June 2005.

Wagner, J.H., Johnson, B.V., Graziani, R.A., Yeh, F.C., 1992. Heat transfer in rotating serpentine passages with trips normal to the flow. J. Turbomach. 114, 847–857.

Watanabe, K., Takahashi, T., 2002. LES simulation and experimental measurement of fully developed ribbed channel flow and heat transfer. In: Proc. ASME Turbo Expo: 2002-GT-30203.

Wilcox, D.C., Chambers, T.L., 1977. Streamline curvature effects on turbulent boundary layers. AIAA J. 15 (4).